The Astrophysical Journal, 596:997–1014, 2003 October 20

SPACE TELESCOPE IMAGING SPECTROGRAPH SLITLESS OBSERVATIONS OF SMALL MAGELLANIC CLOUD PLANETARY NEBULAE: A STUDY ON MORPHOLOGY, EMISSION-LINE INTENSITY, AND EVOLUTION[1]

Letizia Stanghellini[2]
Space Telescope Science Institute, 3700 San Martin Drive, Baltimore, MD 21218;
lstanghe@stsci.edu

Richard A. Shaw
National Optical Astronomy Observatory, 950 North Cherry Avenue, Tucson, AZ 85719;
shaw@noao.edu

Bruce Balick
Department of Astronomy, University of Washington, Seattle, WA 98195;
balick@astro.washington.edu

and

Max Mutchler, J. Chris Blades, and Eva Villaver
Space Telescope Science Institute, 3700 San Martin Drive, Baltimore, MD 21218;
mutchler@stsci.edu, blades@stsci.edu, villaver@stsci.edu
Received 2003 February 21; accepted 2003 June 24

ABSTRACT

A sample of 27 planetary nebulae (PNs) in the Small Magellanic Cloud (SMC) have been observed with the *Hubble Space Telescope* Imaging Spectrograph (*HST*/STIS) to determine their morphology, size, and the spatial variation of the ratios of bright emission lines. The morphologies of SMC PNs are similar to those of LMC and Galactic PNs. However, only a third of the resolved SMC PNs are asymmetric, compared to half of those in the LMC. The low-metallicity environment of the SMC seems to discourage the onset of bipolarity in PNs. We measured the line intensity, average surface brightness, and photometric radius of each nebula in Hα, Hβ, [O III] $\lambda\lambda$4959 and 5007, [N II] $\lambda\lambda$6548 and 6584, [S II] $\lambda\lambda$6716 and 6731, He I λ6678, and [O I] $\lambda\lambda$6300 and 6363. We show that the surface brightness–to-radius relationship is the same as in LMC PNs, indicating its possible use as a distance scale indicator for Galactic PNs. We determine the electron densities and the ionized masses of the nebulae where the [S II] lines were measured accurately, and we find that the SMC PNs are denser than the LMC PNs by a factor of 1.5. The average ionized mass of the SMC PNs is 0.3 $M_{\odot}$. We also found that the median [O III]/Hβ intensity ratio in the SMC is about half that of the corresponding LMC median. We use CLOUDY to model the dependence of the [O III]/Hβ ratio on the oxygen abundance. Our models encompass very well the average observed physical quantities. We suggest that the SMC PNs are principally cooled by the carbon lines, making it hard to study their excitation based on the optical lines at our disposal.

Subject headings: Magellanic Clouds — planetary nebulae: general — stars: AGB and post-AGB — stars: evolution

1. INTRODUCTION

To understand the final phases of stellar evolution of intermediate-mass stars, one has to study the interplay of the stellar and nebular components. During its lifetime, and especially toward the end of its life, a star of mass between 1 and 8 $M_{\odot}$ experiences extreme mass loss and nuclear burning episodes followed by the occurrence of the dredge-ups that change the chemical mix of its envelope. A planetary nebula (PN) is formed by the ejected envelope from a star at the tip of the asymptotic giant branch (AGB), and it can be shaped in part by a fast wind from the remnant during its subsequent evolution.

The process of PN formation and evolution has been studied both theoretically and observationally for decades, yet many fundamental questions remain only partially solved. For example, what is the origin of the different morphologies, and what phenomenon, or series of phenomena, decide the final PN morphology? Does progenitor mass alone dictate the dynamic evolution rate and expansion speed? What is the connection between binary star evolution and the physical properties of PNs (chemistry, morphology, etc.)? What is the role of the interstellar medium (ISM) in PN structure? How much is the nebular gas mix contaminated by the interaction with the ISM? To what extent do PNs enrich C, N, and O in the ISM?

A number of studies based on the comparison of PN and stellar properties with models have shed light on some of these and other questions. Even so, observations of PNs and their central stars are notoriously difficult to compare with adequate theoretical models for a variety of reasons. First, the stellar and nebular components are often observed and analyzed separately, yet they are of common origin; the

[1] Based on observations made with the NASA/ESA *Hubble Space Telescope*, obtained at the Space Telescope Science Institute, which is operated by the Association of Universities for Research in Astronomy (AURA), Inc., under NASA contract NAS 5-26555.

[2] Also affiliated with the ESA Space Telescope Division; on leave from INAF–Osservatorio Astronomico di Bologna.

nebula carries, in its chemical composition, the nuclear burning and dredge-up history of the stellar progenitor, and its morphology carries the signature of the wind history of its central star. Second, the inferred evolutionary times of the stellar and nebular components within the post-AGB phase are unsynchronized. Although theoretical models have been developed to explain the nuclear evolution of the AGB and post-AGB phases, mass-loss rates and geometries of the envelope ejection have not yet been successfully modeled from the stellar viewpoint. Dynamic theoretical models have explained the observed nebular morphology only if ad hoc assumptions are made about the evolution of the central star. Photoionization models are able to predict the strength of optical and UV emission lines that appear during the evolution of PNs, but once again without yielding much insight into the numerous details of the morphology and the evolution of the progenitor star. We believe that only with large samples of well-defined, high-quality data sets that allow the identification and significance of the crucial nebular and stellar physical parameters can one make steps forward in this field of study. Large amounts of data of high quality will be able to constrain the stellar and nebular models, so that open questions on PN formation and evolution may be addressed.

In the quest for acquiring the best observational sets for model testing, PNs in the Magellanic Clouds (SMC, LMC) deserve special attention. LMC and SMC PNs have known distances and low field reddening, in contrast with Galactic PNs. Our aim in the last few years has been that of acquiring and analyzing a large sample of LMC and SMC PN spectra and images that, together with the data existing in the literature, permits the construction of an ideal data set for model testing and for comparison with disk and halo Galactic PNs.

The importance of observing and classifying SMC PN morphology, and of discerning the evolutionary stage of their central stars, is multifold. First, the ambient metallicity of the SMC is closer to that of a primordial galaxy than that of the LMC or the Galaxy, thus making the SMC a unique astrophysical laboratory to study metal-depleted yet resolved stellar populations. Second, by observing a sizable sample of SMC PNs with the *Hubble Space Telescope* (*HST*) (i.e., resolving their morphology and size), we will be able to study the dependence between morphology and abundances in a low-metallicity environment.

The Space Telescope Imaging Spectrograph (STIS) has proved to be a very efficient way to acquire broadband and monochromatic images of PNs smaller than about 2″. In two previous papers of this series (Shaw et al. 2001; Stanghellini et al. 2002), we have presented the results from the STIS slitless spectroscopy of the first set of 29 LMC PNs. In this paper, we present the results relative to the observations of 27 SMC PNs (*HST* program 8663). In § 2, we discuss the observation strategy and the data analysis of this particular observing set; we include there the rationale for target selection, the data calibration, the slitless spectral extraction, the spectral analysis, the photometric radii determinations, and the morphological classification. In § 3, we present the scientific results derived from this set of images and spectra, including the discussion of the line intensity, the surface brightness in the different lines, the excitation of the nebulae, and their optical extinction, all discussed across morphological classes. Section 4 discusses the results so far and the future endeavors in this study. The analysis of the central stars of SMC PNs from the images and spectra of the data set of program 8663 will be discussed in a separate paper.

2. OBSERVATIONS, DATA CALIBRATION, AND ANALYSIS

2.1. *Target Selection and Misclassifications*

Our list of 55 targets was compiled with the intent to obtain data of all known SMC PNs, with accurate coordinates. Most targets came from the Hα survey catalog by Meyssonnier & Azzopardi (1993). The majority of these PNs are bright enough to be observed in snapshot mode (less than 1 *HST* orbit). We included in the target list three objects that have been previously observed with the Wide Field and Planetary Camera 1, and with the Faint Object Camera (FOC). This was done to check the consistency of the morphological classification obtained with archived instruments and the STIS.

Our *HST* observations were performed in snapshot mode. The targets were selected from the original list by the scheduling specialists at STScI, according to the available observing slots. Typically, shorter exposures (i.e., brighter targets) are favored. The program was completed at the 53% level, which is normal for a successful snapshot proposal. Among the 29 targets observed (Table 1), 27 are the SMC PNs analyzed in this paper. Two (MG 2 and MA 1796) are misclassified H II regions, whose images and analysis will be published in another paper. As it turned out, faint targets are slightly underrepresented in our sample.

2.2. *Observing Technique*

The observations were acquired with STIS. All observations were made with the CCD detector in direct imaging (50CCD) and slitless modes. The spatial scale of the CCD is 0.″051 pixel^{-1}, corresponding to 0.014 pc pixel^{-1} at the distance of the SMC. This allows a very good spatial resolution to study PN morphology and size, comparable to what used in ground-based imaging observations of Galactic PNs.

Each imaging observation was split in two, to allow easy cosmic-ray removal. The slitless spectra were acquired with the G430M and G750M gratings for most nebulae. Observations with the G430M grating cover the range 4818–5104 Å at 0.28 Å pixel^{-1}, and those with the G750M grating cover the range 6295–6867 Å at 0.56 Å pixel^{-1}. The exposures were planned to have a good signal-to-noise ratio in the [O III] λ5007 and Hα lines. Several additional lines have been detected in many PNs, including Hβ and [O III] λ4959, using G430M, and [O I] $\lambda\lambda$6300, 6363, [S III] λ6312, [N II] $\lambda\lambda$6548, 6584, He I λ6678, and [S II] $\lambda\lambda$6716, 6731, using G750M. In some cases the G430M exposures were skipped, limited by the *HST* snapshot duration.

The observing log is reported in Table 1, where we list the targets, the observing date, the data set name, the spectral element used in the observations, and the exposure time and number of exposures obtained. Aliases are identified in the table notes. The STIS data were calibrated using the standard pipeline system, as in the LMC data (Shaw et al. 2001).

Figures 1–6 show the observed SMC PNs in the three observing modes: left-hand panels show the broadband CCD images, middle panels show the Hα and [N II] images, and right-hand panels show, when available, the [O III] λ5007 images.

TABLE 1

Observing Log for SMC Planetary Nebulae

Nebula	Date	Data Set	Disperser	T_{exp} (s)	N_{exp}
J4	2000 Aug 18	O65S03030	G430M	840	2
		O65S03020	G750M	890	2
		O65S03010	MIRVIS	300	2
J18	2000 Oct 3	O65S08020	G750M	2100	2
		O65S08010	MIRVIS	300	2
J23	2000 Aug 8	O65S12020	G750M	2100	2
		O65S12010	MIRVIS	300	2
J27	2000 Oct 10	O65S16020	G750M	2100	2
		O65S16010	MIRVIS	300	2
MA 1682	2000 Nov 5	O65S24020	G750M	2100	2
		O65S24010	MIRVIS	300	2
MA 1762	2000 Aug 19	O65S25020	G750M	2100	2
		O65S25010	MIRVIS	300	2
MA 1796	2000 Sep 27	O65S26040	G430M	200	2
		O65S26020	G750M	100	2
		O65S26030	G750M	400	2
		O65S26010	MIRVIS	120	2
		O65S26KGQ	MIRVIS	15	2
MG 2	2000 Nov 7	O65S28030	G430M	800	2
		O65S28020	G750M	1300	2
		O65S28010	MIRVIS	300	2
MG 8	2000 Nov 7	O65S34030	G430M	1200	2
		O65S34020	G750M	620	2
		O65S34010	MIRVIS	120	2
MG 13	2000 Sep 28	O65S39020	G750M	2100	2
		O65S39010	MIRVIS	300	2
SMP 1	2001 Feb 6	O65S40030	G430M	360	2
		O65S40020	G750M	170	2
		O65S40010	MIRVIS	120	2
SMP 4	2001 Jan 9	O65S41030	G430M	460	2
		O65S41020	G750M	230	2
		O65S41010	MIRVIS	120	2
SMP 6	2001 Mar 9	O65S42030	G430M	280	2
		O65S42020	G750M	190	2
		O65S42010	MIRVIS	120	2
SMP 8	2001 Jan 23	O65S43030	G430M	320	2
		O65S43020	G750M	160	2
		O65S43010	MIRVIS	120	2
		O65S43GKQ	MIRVIS	15	1
SMP 9[a]	2000 Nov 20	O65S02030	G430M	1100	2
		O65S02020	G750M	790	2
		O65S02010	MIRVIS	300	2
SMP 11[a]	2000 Sep 6	O65S05040	G430M	200	2
		O65S05020	G750M	60	2
		O65S05030	G750M	300	2
		O65S05010	MIRVIS	120	2
		O65S05LBQ	MIRVIS	15	1
SMP 12	2000 Oct 14	O65S44030	G430M	650	2
		O65S44020	G750M	810	2
		O65S44010	MIRVIS	300	2
SMP 13[a]	2000 Nov 20	O65S06040	G430M	52	2
		O65S06020	G750M	36	2
		O65S06030	G750M	180	2
		O65S06010	MIRVIS	120	2
		O65S06CHQ	MIRVIS	15	1
SMP 14	2000 Sep 17	O65S45030	G430M	540	2
		O65S45020	G750M	290	2
		O65S45010	MIRVIS	120	2
SMP 17	2001 Jan 16	O65S47040	G430M	160	2
		O65S47020	G750M	100	2
		O65S47030	G750M	100	2
		O65S47010	MIRVIS	120	2
		O65S47FXQ	MIRVIS	15	1
SMP 18[a]	2001 May 16	O65S09040	G430M	160	2
		O65S09020	G750M	42	2
		O65S09030	G750M	210	2
		O65S09010	MIRVIS	120	2
		O65S09JIQ	MIRVIS	15	1
SMP 19[a]	2000 Oct 14	O65S10030	G430M	330	2
		O65S10020	G750M	260	2
		O65S10010	MIRVIS	120	2
SMP 20	2001 Jan 21	O65S48040	G430M	160	2
		O65S48020	G750M	80	2
		O65S48030	G750M	320	2
		O65S48010	MIRVIS	120	2
		O65S48YXQ	MIRVIS	15	1
SMP 22	2000 Oct 14	O65S49030	G430M	840	2
		O65S49020	G750M	200	2
		O65S49010	MIRVIS	120	2
SMP 23[a]	2000 Oct 14	O65S15030	G430M	230	2
		O65S15020	G750M	380	2
		O65S15010	MIRVIS	120	2
SMP 24	2001 Mar 9	O65S50030	G430M	500	2
		O65S50020	G750M	150	2
		O65S50010	MIRVIS	120	2
SMP 25	2001 Mar 5	O65S51030	G430M	920	2
		O65S51020	G750M	460	2
		O65S51010	MIRVIS	120	2
SMP 26	2000 Sep 28	O65S52030	G430M	1200	2
		O65S52020	G750M	900	2
		O65S52010	MIRVIS	300	2
SMP 27	2001 Jan 19	O65S53040	G430M	160	2
		O65S53020	G750M	80	2
		O65S53030	G750M	360	2
		O65S53010	MIRVIS	120	2
		O65S53QBQ	MIRVIS	15	1
SP 34	2000 Oct 14	O65S55030	G430M	1000	2
		O65S55020	G750M	500	2
		O65S55010	MIRVIS	300	2

[a] SMP 9 = J3; SMP 11 = J8; SMP 13 = J11; SMP 18 = J19; SMP 19 = J20; SMP 23 = J26.

2.3. *One-dimensional Spectral Extraction and Line Intensities*

Spectral analysis of the SMC PNs has been performed similarly to that of LMC PNs (Stanghellini et al. 2002). For most PNs observed, the combination of dispersion and spatial scale allows a clear separation of the monochromatic images for all emission lines. Exceptions are J27, where broad and monochromatic images are at the limit of detectability, and MA 1682, where the [N II] and Hα images may have partial overlap. No images are severely overlapped; thus, the one-dimensional spectral extraction was adequate for nebular line flux and ratio analysis. We extracted the one-dimensional spectra and applied a photometric calibration, using the standard STIS calibration pipeline module *x1d* (McGrath, Busko, & Hodge 1999). We used extraction boxes for the nebulae large enough to encompass all the nebular features, but snug enough to exclude most of the sky background from the extraction. Sky background regions were selected for each object to avoid stray stellar photons from field stars. The background was then averaged and subtracted.

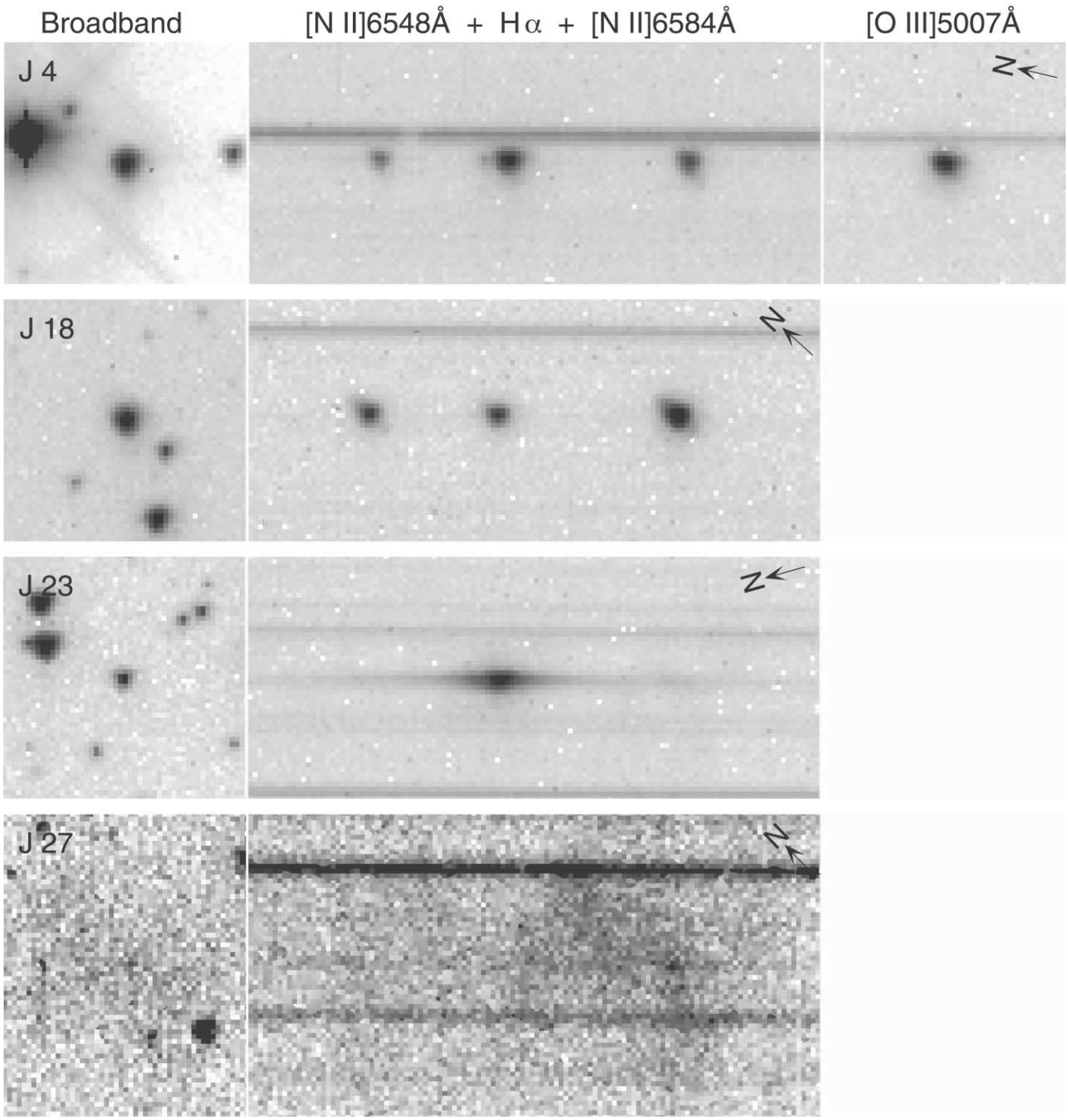

FIG. 1.—STIS images of the LMC PNs J4, J18, J23, and J27 with a logarithm intensity scale. From left to right, we show for each PN the broadband image, the [N II]–Hα section of the G750M spectrum, and the [O III] λ5007 image of the G430M spectrum, when available.

We measured emission-line intensities with IRAF[3] *splot* task, fitting Gaussians to individual lines, while estimating the continuum level. In the cases in which the emission lines were notably non-Gaussian, we estimated the line flux as measured from the area above the continuum.

[3] IRAF is distributed by the National Optical Astronomical Observatory, which is operated by the Association of Universities for research in Astronomy (AURA), Inc., under cooperative agreement with the National Science Foundation.

In Table 2, we report the measured line intensities for the SMC PNs in our sample. Column (1) gives the common names; column (2) gives the logarithmic Hβ intensities, not corrected for extinction, in ergs cm^{-2} s^{-1}; column (3) lists the logarithmic optical extinction at Hβ (Osterbrock 1989); columns (4)–(14) give the line intensities for each nebula, relative to H$\beta = 100$, not corrected for extinction. Line identification are given at the heads of the columns.

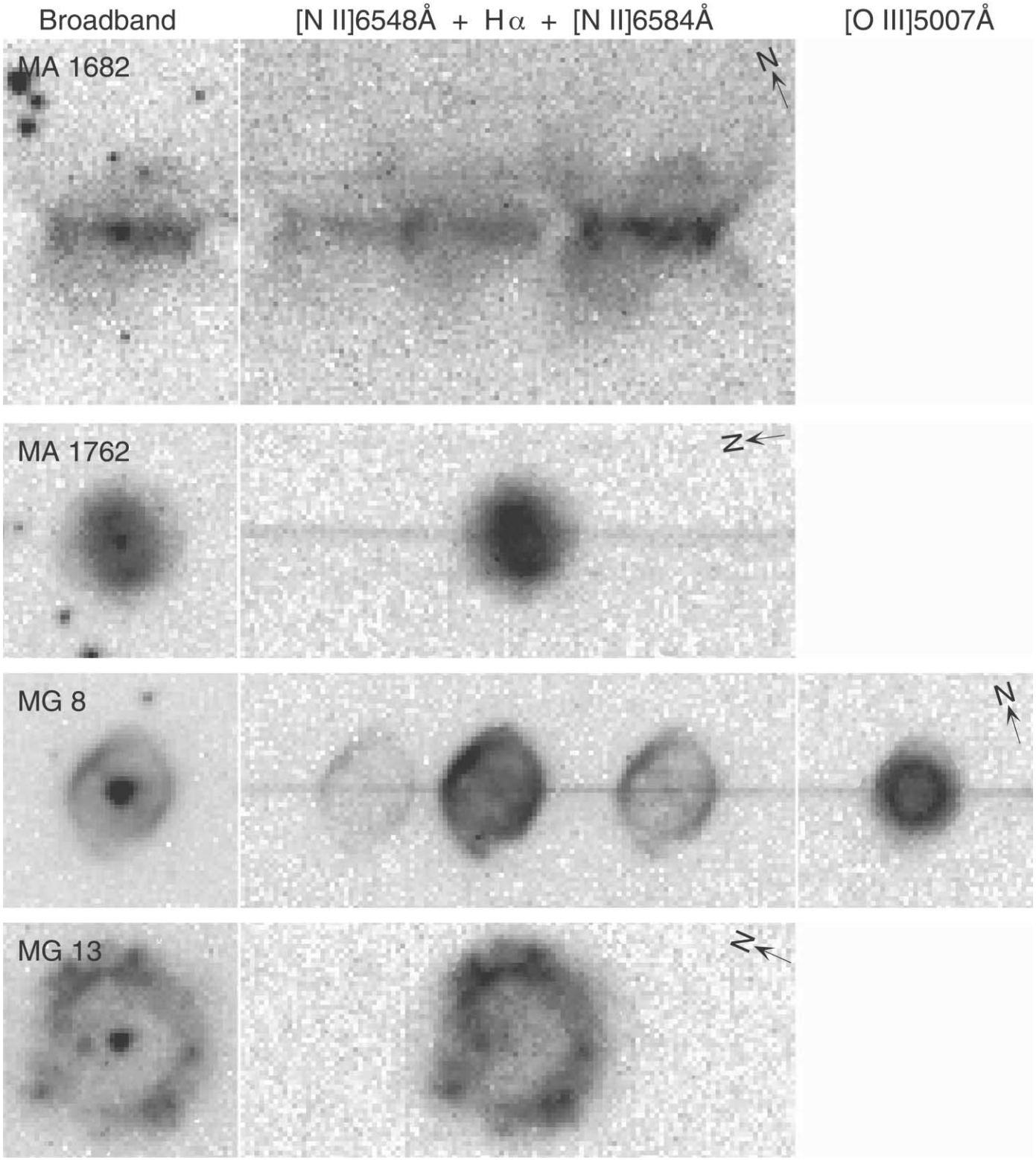

FIG. 2.—Same as Fig. 1, but for MA 1682, MA 1762, MG 8, and MG 13

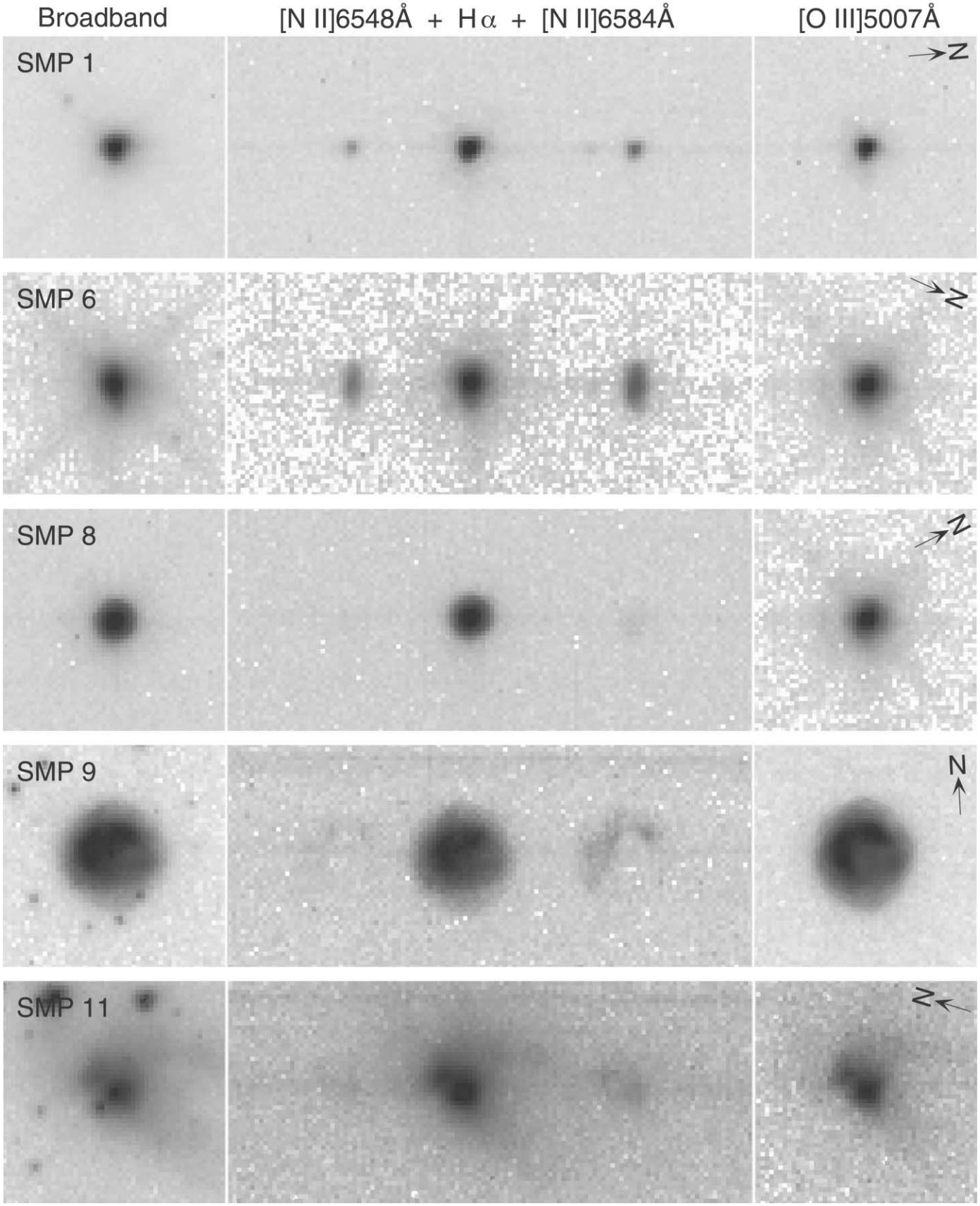

FIG. 3.—Same as Fig. 1, but for SMP 1, SMP 6, SMP 8, SMP 9, and SMP 11

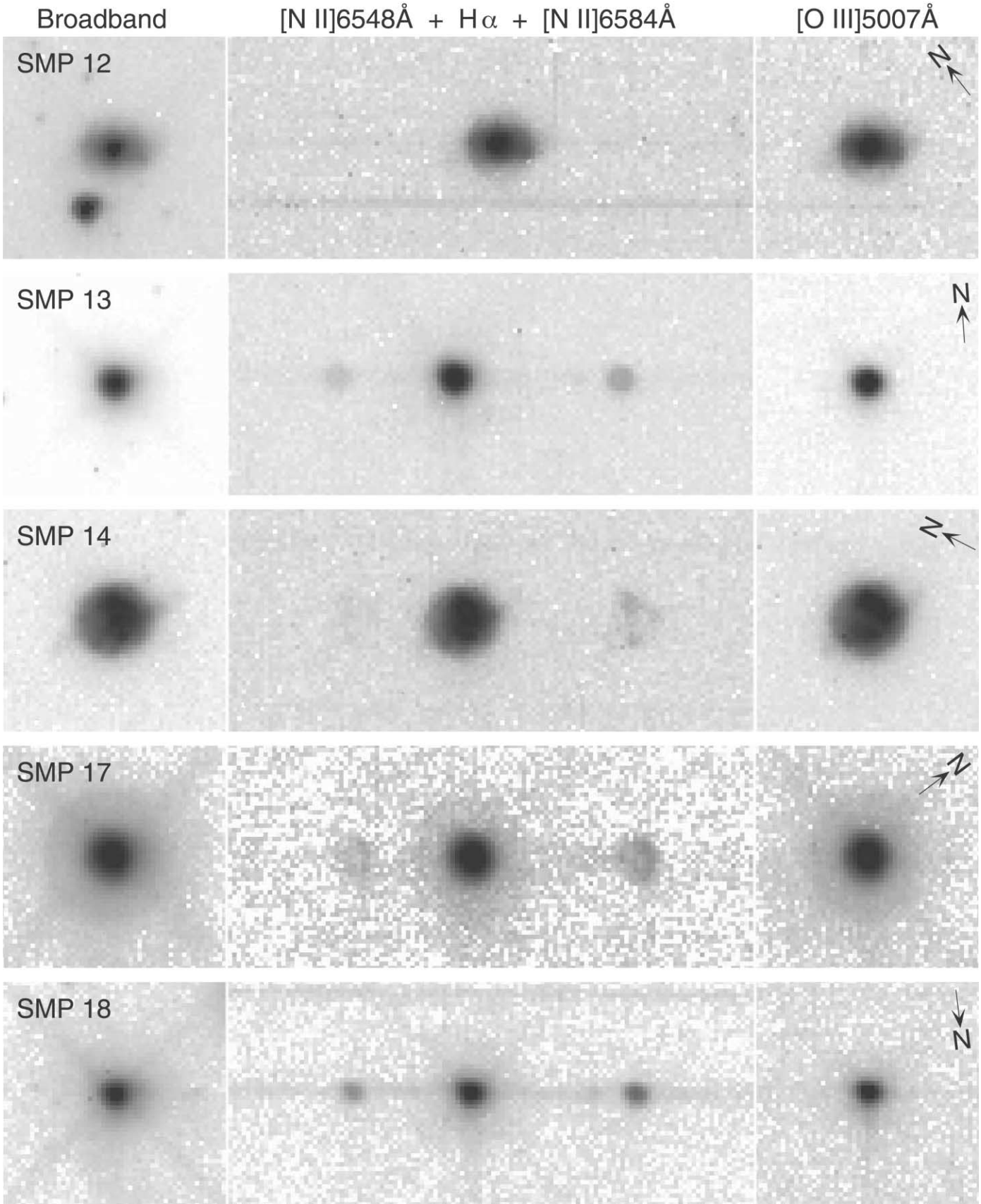

FIG. 4.—Same as Fig. 1, but for SMP 12, SMP 13, SMP 14, SMP 17, and SMP 18

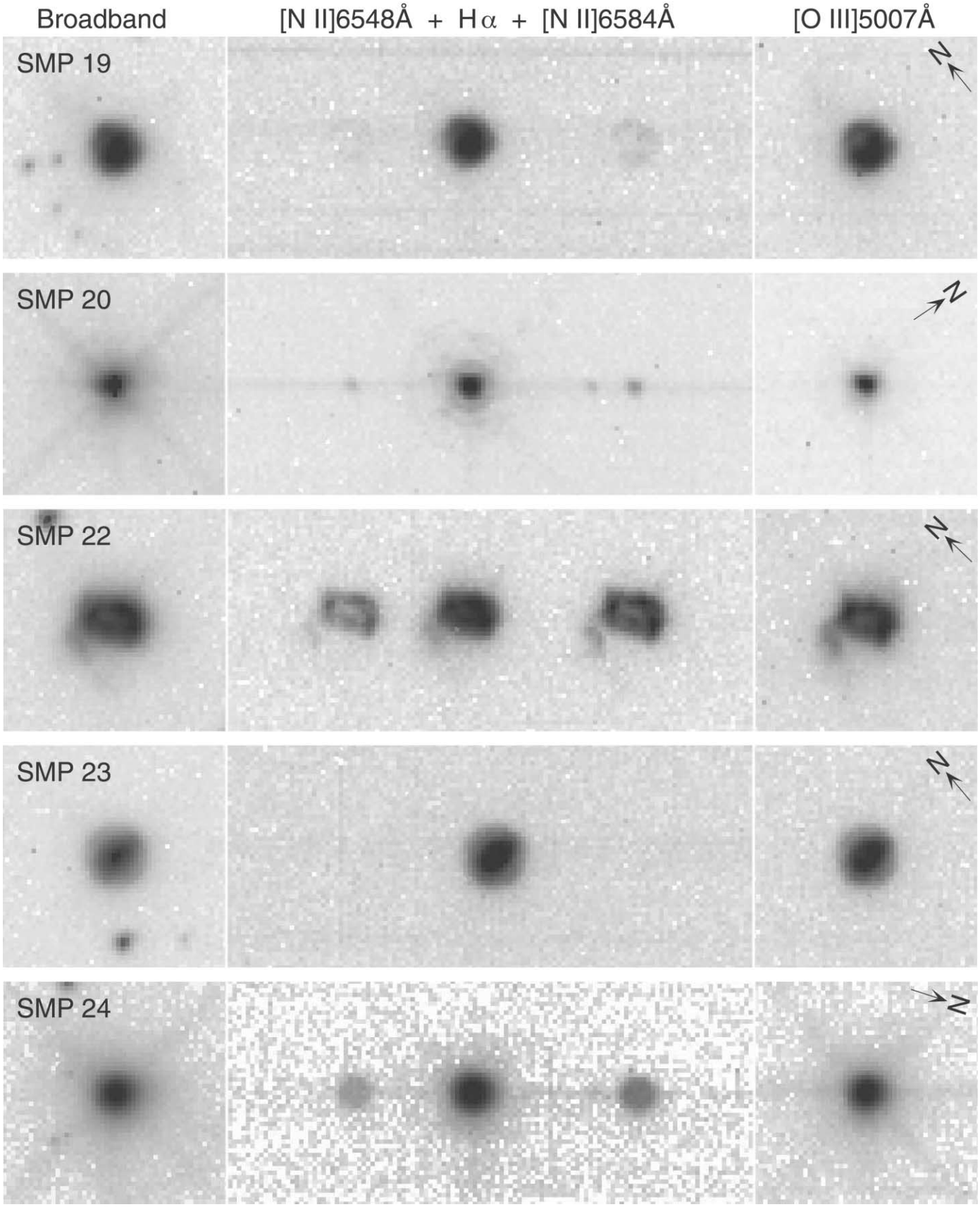

FIG. 5.—Same as Fig. 1, but for SMP 19, SMP 20, SMP 22, SMP 23, and SMP 24

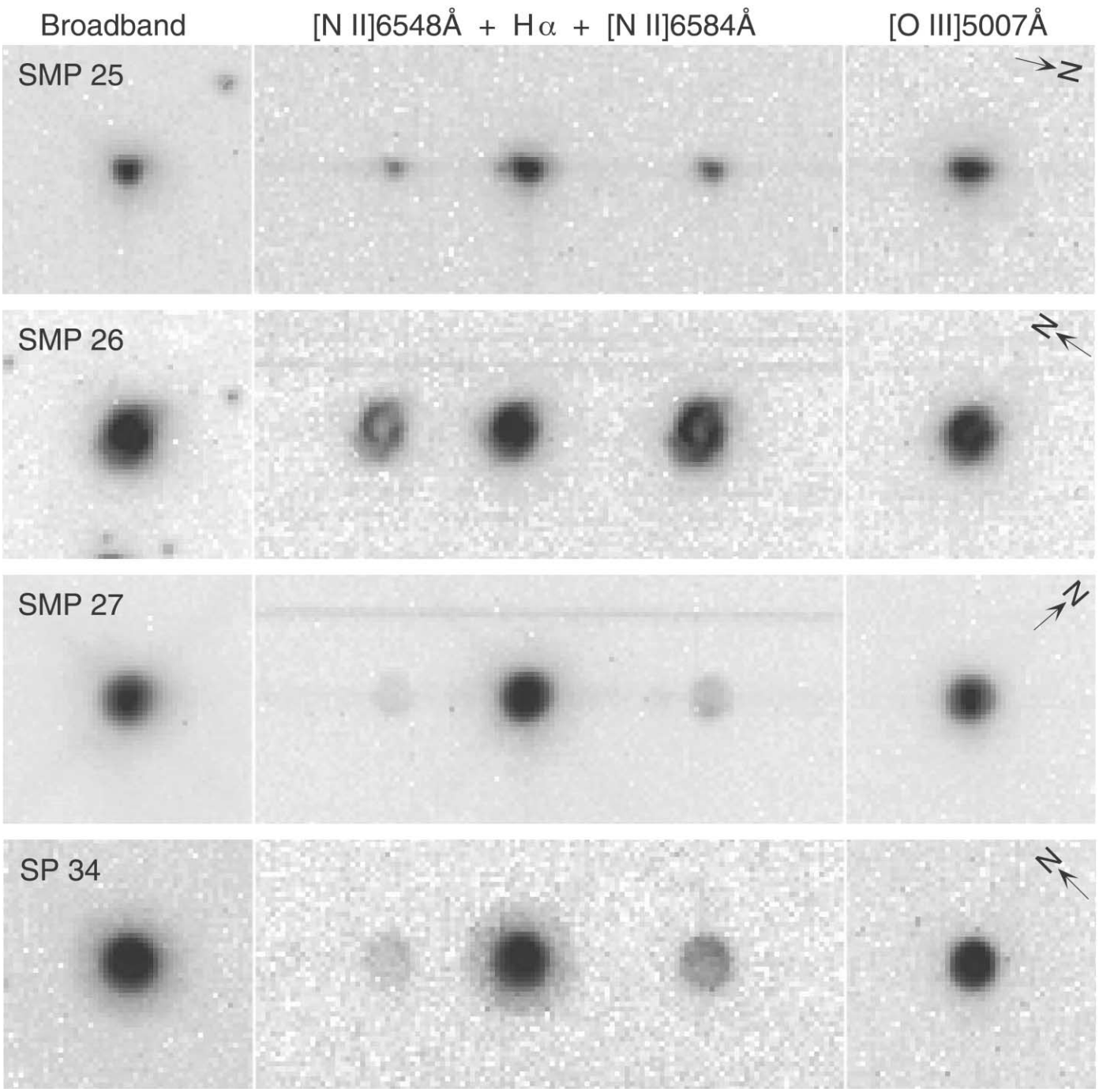

FIG. 6.—Same as Fig. 1, but for SMP 25, SMP 26, SMP 27, and SP 34

From the analysis of our spectral line measurements, and given the similarities of this data set to the ones analyzed in Stanghellini et al. (2002), we confirm that the errors in the line intensities of Table 2 ($\delta \log F$) are (in dex)

$$\delta \log F < 0.05 \quad \text{if} \quad \log F > -12.25 ;$$
$$\delta \log F < 0.15 \quad \text{if} \quad -12.25 > \log F > -12.75 ;$$
$$\delta \log F < 0.2 \quad \text{if} \quad -12.75 > \log F > -13.5 ;$$
$$\delta \log F < 0.25 \quad \text{if} \quad -13.5 > \log F > -14.5 ;$$
$$\delta \log F < 0.55 \quad \text{if} \quad \log F < -14.5 .$$

In Figure 7, we compare the measured line intensities with those available in the literature. We used the data from selected references (Dopita & Meatheringham 1990, 1991a, 1991b; Vassiliadis et al. 1992). Some authors give the intensity corrected for extinction, so before comparison to the present results we uncorrect the intensity ratios by using the extinction constant given in the same reference. We have comparisons for several emission lines in MG 8, MG 13, SMP 1, SMP 6, SMP 11, SMP 13, SMP 14, SMP 17, SMP 25, and SMP 26. A comparison of our fluxes to previous values (Fig. 7) shows a generally good agreement. The correlation

TABLE 2

RELATIVE EMISSION-LINE INTENSITIES OF SMC PLANETARY NEBULAE

Nebula (1)	$F(H\beta)$ (λ4861) (ergs cm^{-2} s^{-1}) (2)	c (3)	[O III] λ4959 (4)	[O III] λ5007 (5)	[O I] λ6300 (6)	[S III] λ6312 (7)	[O I] λ6363 (8)	[N II] λ6548 (9)	Hα λ6563 (10)	[N II] λ6584 (11)	He I λ6678 (12)	[S II] λ6716 (13)	[S II] λ6731 (14)
J4	−13.55	0.168	159.1	480.4	5.1	3.8	2.5	28.9	326.3	102.5	1.9	1.6	3.0
J18	−13.90[a]	...	...	...	1.736	...	...	107.2	100	330.4	...	4.2	2.928
J23	−13.19[a]	...	...	...	...	...	...	...	100	13.9	...	...	...
J27	−14.05[a,b]	...	...	...	...	...	...	...	100	...	...	...	...
MA 1682	−14.17[a]	...	...	...	...	...	...	...	100	304.5	...	...	...
MA 1762	−13.36[a]	...	...	...	0.7829	...	...	...	100	...	...	...	...
MG 8	−13.27	0.133	41.4	126.5	2.0	1.6	...	22.9	317.2	98.3	4.7	5.3	22.0
MG 13	−13.10[a]	...	...	...	...	...	...	...	100	...	...	...	...
SMP 1	−12.85	0.287	85.0	262.1	2.0	0.9	0.7	8.9	359.3	25.7	4.3	0.3	0.7
SMP 6	−12.80	0.385	267.7	791.1	7.0	1.9	1.6	13.7	388.6	44.5	5.3	0.8	1.6
SMP 8	−12.81	0.026	198.7	592.3	...	...	...	1.3	291.0	2.5	3.6	...	...
SMP 9	−13.46	0.070	318.8	959.4	1.4	1.6	...	8.1	301.4	23.5	...	9.7	6.8
SMP 11	−13.13	0.352	110.9	351.4	5.0	...	...	10.0	378.6	28.5	3.9	3.3	8.0
SMP 12	−13.59	0.056	203.5	613.3	...	...	...	...	298.0	...	3.5	...	...
SMP 13	−12.59	0.190	277.3	828.1	2.8	0.8	1.0	2.9	332.0	8.8	3.9	0.8	1.3
SMP 14	−13.04	0.069	311.1	928.8	2.6	1.1	1.0	4.4	301.2	10.2	1.0	1.8	3.0
SMP 17	−12.55	0.064	294.0	893.2	2.8	0.3	1.2	3.7	300.0	7.6	4.0	1.1	0.5
SMP 18	−12.66	0.122	105.0	309.0	1.3	0.7	0.4	7.3	314.5	24.0	3.6	0.4	0.7
SMP 19	−13.04	0.161	282.4	847.2	4.0	1.2	0.9	3.4	324.5	7.7	2.4	1.5	2.2
SMP 20	−12.47	−0.019	143.8	434.9	...	...	...	1.0	280.8	2.8	3.9	...	...
SMP 22	−12.94	0.165	99.1	298.2	14.8	...	5.6	87.7	325.4	259.6	2.9	9.8	14.3
SMP 23	−13.18	0.101	271.5	828.1	...	...	...	...	309.2	3.6	3.6	...	...
SMP 24	−12.66	0.047	137.9	420.1	1.9	0.9	...	6.2	295.9	18.8	4.0	2.1	2.5
SMP 25	−13.28	0.100	108.8	328.2	3.2	1.6	...	15.8	309.0	47.6	5.6	1.3	1.9
SMP 26	−13.58	0.253	205.0	613.0	19.7	...	5.2	111.1	349.4	327.2	2.0	14.8	17.7
SMP 27	−12.51	0.040	188.8	580.1	1.4	0.5	0.4	1.8	294.2	5.2	3.8	0.2	0.6
SP 34	−13.67	0.163	162.8	488.4	12.7	...	22.4	19.0	325.1	55.8	...	14.3	14.6

[a] The Hβ flux is not available for this target. We give the Hα flux instead. All line ratios are calculated with respect to $F_{H\alpha} = 100$ for this PN.

[b] This measurement include the Hα and [N II] blended fluxes.

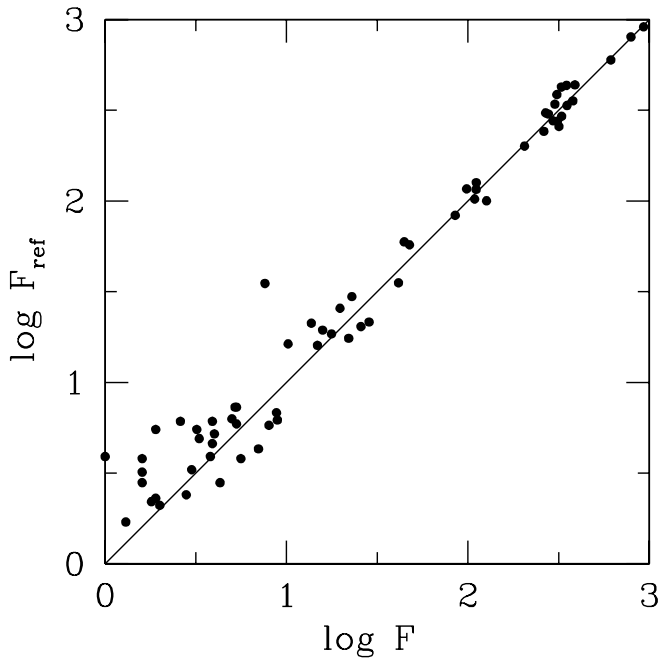

FIG. 7.—Comparison of the measured line intensity ratios with those in the literature, in logarithmic scale.

coefficient between the two sets of fluxes is 0.994, with rms scatter of 0.2 dex. Uncertainties in the reference fluxes are typically quoted at 20%–50%, with higher uncertainties for lower fluxes while our errors are generally smaller (Stanghellini et al. 2002). The outlying point in Figure 7 corresponds to the [N II] λ6584 flux measurement of target SMP 17. We believe that our measurement is correct, since the reddened [N II] λ6584/λ6548 intensity ratio is 2 : 1, while the reference does not detect the [N II] λ6548 line.

3. RESULTS

3.1. *Dimensions and Morphology of SMC Planetary Nebulae*

In Table 3, columns (2) and (3), we give the positions of the central stars (CSs) of the nebulae from the continuum images, where observed. Alternately, we give the geometric center positions of the PNs. Columns (4) and (5) of Table 3 give the photometric radii of the nebulae, measured as described in Stanghellini et al. (1999), and the nebular dimensions, measured from the 10% brightness contour.

Figures 1–6 show the SMC PN images, exhibiting the same range of morphological types as those of LMC and Galactic PNs. The morphological classification used in this paper is the same as that in the other papers of this series (Shaw et al. 2001; Stanghellini et al. 2002): we classify PNs as round (R), elliptical (E), bipolar core (BC), bipolar (B), and point-symmetric (P). We distinguish between round

TABLE 3

POSITIONS, DIMENSIONS AND MORPHOLOGIES OF SMC PLANETARY NEBULAE

Nebula (1)	R.A. (J2000.0) (2)	Decl. (J2000.0) (3)	R_{phot} (arcsec) (4)	Dimensions (arcsec) (5)	Morphological Classification (6)	Notes (7)
J4	00 45 27.30	−73 42 15.3	0.32	0.27	E	Possible ansae
J18[a]	00 51 43.39	−73 00 54.1	0.17	0.14	R?	Elongated in [N II]
J23[a]	00 55 30.52	−72 50 21.3	0.38	...	...	Broad Hα emission; unresolved
J27[a]	00 59 43.48	−72 57 17.9	...	2.5 × 1.7	B?	Very low surface brightness
MA 1682[a]	01 09 03.52	−72 29 05.2	0.83	2.86 × 2.17	B	
MA 1762[a]	01 12 40.28	−72 53 46.4	0.71	1.45 × 1.26	E(bc)	
MG 8	00 56 19.59	−72 06 58.5	0.48	1.39 × 1.28	E	Inner structure
MG 13[a]	01 43 10.33	−72 57 03.2	1.55	1.22 × 1.09	E	Inner structure
SMP 1	00 23 58.67	−73 38 03.8	0.15	...	...	Unresolved
SMP 6	00 41 27.52	−73 47 06.2	0.19	...	E	
SMP 8	00 43 25.17	−72 38 18.9	0.23	0.41 × 0.38	R	
SMP 9	00 45 20.66	−73 24 10.5	0.55	1.20	R	Inner structure
SMP 11	00 48 36.61	−72 58 00.1	0.99	0.78 × 0.66	B	Possible inner ring
SMP 12	00 49 21.00	−73 52 58.0	0.37	0.78 × 0.51	E	
SMP 13	00 40 51.71	−73 44 21.3	0.19	0.20	R	
SMP 14	00 50 34.99	−73 42 57.9	0.42	0.83	R	Ansae and/or inner structure
SMP 17	00 51 56.41	−71 24 44.6	0.25	0.50	E	Faint detached 1″.5 halo; inner ring in [N II]
SMP 18	00 51 57.97	−73 20 30.1	0.15	0.14	...	Unresolved
SMP 19	00 53 11.14	−72 45 07.5	0.30	0.59	R	Outer structure
SMP 20	00 56 05.39	−70 19 24.7	0.15	0.20 × 0.23	...	Unresolved
SMP 22	00 58 37.44	−71 35 49.1	0.40	0.71 × 0.54	B?	Possible ansae
SMP 23	00 58 42.14	−72 56 59.6	0.30	0.66 × 0.60	E(bc)	
SMP 24	00 59 16.09	−72 01 59.7	0.20	0.38	E	
SMP 25	05 30 33.22	−70 44 38.4	0.19	...	E	
SMP 26	01 04 17.81	−73 21 51.2	0.28	0.61 × 0.57	P	
SMP 27	01 21 10.67	−73 14 35.4	0.23	0.45	R	Attached outer halo
SP 34	01 12 10.76	−71 26 50.2	0.61	0.71 × 0.69	R	Attached outer halo

NOTE.—Units of right ascension are hours, minutes, and seconds, and units of declination are degrees, arcminutes, and arcseconds.

[a] No [O III] image available.

and elliptical if the axial ratio is larger than unity by at least 10%. Bipolarity follows the classic definition (Stanghellini, Corradi, & Schwarz 1993), while bipolar core is defined in Stanghellini et al. (1999). Note that bipolar core PNs of this sample are defined as such only if their BC is apparent above the 10% intensity contour. Morphology is based primarily on the Hα images and differs only rarely from that based on the [O III] λ5007 images (Manchado et al. 1996). Column (6) of Table 3 gives the morphological classification. In a couple of cases, we use the terminology of round and elliptical PNs with inner structures. These structures may be bipolar cores, although we believe that we have the necessary spatial resolution to make the distinction. Question marks indicate that the morphological determination is ambiguous or uncertain. In the following paragraphs, we describe in detail the morphological types of our sample PNs.

J4 (*E*).—The field is crowded, making the identification on the clear image a little uncertain. The spectrum is reasonably well exposed and shows emission in the full set of emission lines. The nebular morphology is elliptical. We detected extremely faint emission in the [O III] frame up to 1.″42 from the center of the PN in the spatial direction.

J18 (*R*).—This PN is round in Hα and has an elliptical shape in [N II]. It does not show a bipolar core. The [N II] λ6584 emission is brighter than the Hα.

J23.—This object is apparently spatially unresolved, and its identification on the clear image is difficult. The stellar spectrum shows strong and broad Hα and a weaker [N II] λ6584 line. We also detect He I λ6678. The Hα velocity width appears to be about 200–300 km s^{-1}, which is broad for a PN. This object could not be a common symbiotic star; it would have a giant companion with an unusually bright Hα emission line and a faint underlying continuum (Boroson & Liebert 1989).

J27 (*B?*).—This object is roughly box-shaped and may be the remnant of a bipolar. The nebula is barely detected in the broadband exposure, at roughly 20 counts pixel^{-1} above the background. The spectrum shows faint [N II] emission, with some hint of Hα emission. No CS is detected.

MA 1682 (*B*).—This is an extreme bipolar PN, with a prominent central torus seen edge-on. The Hα and [N II] lines are very strong in the spectrum, and [S II] is barely detected; no other lines are detected. We do not have a blue spectrum. The CS is easily detected in the continuum image.

MA 1762 [*E*(*bc*)].—This is an elliptical PN with a binebulous inner core. We detected Hα and, marginally, [O I] λ6300. The CS is easily detected in the continuum image and in the spectrum.

MG 8 (*E*).—This elliptical PN has a very distinct ring structure, with a hint of ansae (or arms) that extend 0.″1 along the major axis from the 10% contour. The armlike structure leads to a point-symmetric classification, but to be conservative we classify this as elliptical, possibly bipolar core. Hα is very strong, [N II] is apparent but weaker, [S II] is very weak, and we could also detect a trace of the [O I] λ6300 emission. Hβ is well exposed, and [O III] is only a bit stronger. The morphology in [O III] differs in detail from the Hα and other line morphology, in that the emission comes primarily from a ring that is inside the emission from most other lines. The CS is exceptionally bright in the continuum image; could it be a binary companion to the true CS?

MG 13 (*E*).—This elliptical PN has a very knotty ring structure and is classified as E(s). Hα is very strong, but neither [N II] nor any other line is detected in the G750M spectrum. The CS is easily detected in the continuum image.

SMP 1.—Marginally resolved round or elliptical PN with no detected image of the CS. Most emission lines are present, and there may be a trace of He I at 4927 Å as well. The [S II] lines are marginally detected.

SMP 6 (*E*).—The [N II] morphology is slightly different from that of the other lines, in that it shows a larger elongation.

SMP 8 (*R*).—This round PN has very strong Hα and [O III] emission, with [N II] and He I at the 1% level and [S II] weaker still. [O I] is marginally detected at 6300 Å. The CS is detected in the continuum image, but there is a significant contribution from the nebular emission.

SMP 9, or J3 (*R*).—This round PN has a bright hemisphere of emission to the northeast, making the whole somewhat asymmetric in appearance. We are not sure that the inner structure clearly discloses a bipolar core, but there is a lot of structure. Hα and [O III] are very strong, but [N II] is fairly weak. The asymmetry is pronounced in the [N II] lines. [S II] and He I are also present but very weak, and [O I] λ6300 may be marginally detected. The CS has been detected in the continuum image.

SMP 11, or J8 (*B*).—This complex bipolar PN has a distinct dark band that divides the bright core into two unequal lobes. This looks very much like a case of a strong bipolar ring, viewed some distance from the plane. A faint bipolar structure is even evident up to 2″ from the center (particularly to the south), but the ribbed, fanlike structure is projected off-center on the sky, and [N II] λ6548 is blended with the Hα Gaussian wing. Hα and [O III] are very strong, but [N II] λ6584 is fairly weak; these lines all show the same morphological structures. [S II] and He I are also present but very weak, and [O I] λ6300 is also detected. The CS is detected in the continuum image and possibly also in the G750M spectrum.

SMP 12 (*E*).—Elliptical PN with a detected CS. The central emission shows some structure (Es). In the [O III] image there is a hint of extended lobe to the east.

SMP 13, or J11 (*R*).—The appearance of this PN is nearly stellar in the continuum but appears very mildly elliptical in the ionization lines. We classify it as round, since the ellipticity is below the 10% level. Faint emission in the [O III] image is detected up to 1.″42 from the geometrical center. Hα and [O III] are very strong; [N II], He I, and [S II] are very weak but detected. Also weak are [O I] $\lambda\lambda$6300, 6363 and [S III] λ6312. The CS may be detected in the continuum image.

SMP 14 (*R*).—This round PN has a distinct structure in the inner core and faint ansae that extend 0.″3 from the 10% contour. Hα is very strong, and [N II] is detected in the spectrum but is very weak. [S II] and He I are also present but weak. [O III] is quite strong. The CS is easily detected in the continuum image.

SMP 17 (*E*).—This is an elliptical PN, with a very faint outer halo that is detected in the continuum image, in Hα, and in [O III] at the 0.4% contour level, out to about 1.″3. The inner portion is somewhat elliptical in all the observed lines except [N II], where it is ringlike. The [O III] emission shows a marginal bipolar core. Hα is very strong, and [N II] is present but very weak. The CS is detected in the continuum image, but there is a significant contribution from the nebular emission.

SMP 18, or J19.—This is a small PN with bright Hα and [O III] emission. The extension is smaller in [N II] than in the

other lines. It is barely resolved when compared to the broadband images of the stars.

SMP 19, or J20 (*R*).—Morphologically similar to J3, the inner parts of this PN are slightly distorted in the [O III] lines and Hα. We classify it as round with structures. There is outer emission of 1″ radius.

SMP 20.—This PN is bright but unresolved. Hα and [O III] are very strong, with [N II] at the 1% level and He I, [S II], and [O I] weaker still. The CS is detected in the continuum image, but there is a significant contribution from the nebular emission. The stellar spectrum shows a feature at about 6577 Å, which is also seen in a few other targets in our sample.

SMP 22 (*B?*).—This PN has a very interesting box/ring shape, with a possible emission "arm" toward the east that is very evident in the [N II] images (could it be part of the ISM?). It is classified as bipolar. There are at least three high-emission features within the ring. The line profiles of all lines but Hα and Hβ are split, showing the ring morphology.

SMP 23, or J26 [*E*(*bc*)].—Elliptical PN with a bipolar core.

SMP 24 (*E*).—An elliptical PN in the Hα and [O III] emission lines, it shows some small-scale structures in the light of [N II]. This nebula may have a faint halo.

SMP 25 (*E*).—Elliptical PN with a likely broad stellar Hα emission line.

SMP 26 (*P*).—This PN could be point-symmetric, with two arms that extend from the northeast and southwest of the center. It is possible that this PN is elliptical, with low-ionization ansae. Hα is fairly strong, but [N II] is nearly as bright and shows the arms much more clearly. The line profiles in the one-dimensional spectra are split in all lines except Hα. No CS is detected in the continuum image.

SMP 27 (*R*).—This is a (very low ellipticity) elliptical PN. There is a hint of structure in the [N II] images only. Hα and [O III] are very strong, with [N II] at the 1% level and He I, [S II], and [O I] weaker still. The CS is detected in the continuum image, but there is a significant contribution from the nebular emission.

SP 34 (*R*).—This is a round PN, with a faint outer halo that is detected in the continuum image and in Hα at the 5% contour level. The inner portion shows significant asymmetry in all the observed lines, in that the western edge is much brighter. Hα is fairly strong, and [N II] is present but much weaker. No CS is detected in the continuum image.

3.2. *Targets in Common with Prior HST Programs*

We included in our STIS target list three objects that were previously observed with the Planetary Camera 1 (PC1) and the FOC. The rationale to include a few repeat targets from the sample of Stanghellini et al. (1999) was to check the morphological types and dimensions with both methods and to asses the reliability of the pre-COSTAR archival data. All three were observed before the first *HST* servicing mission; thus, the images suffer for the uncorrected spherical aberration of the telescope mirror. In an *HST* archival study (Stanghellini et al. 1999), it was found that morphology was well determined with the archived instruments, while dimensions of the nebulae with the photometric method were not always reliable because of the possible presence of fainter extended halos around the images.

Since program 8366 was a snapshot program, we could not guarantee exactly which targets would be observed for this comparison. In the end, targets SMP 1 (N1), SMP 6 (N6), and SMP 22 (N67) were reobserved with STIS. The first two targets were observed with PC1 earlier, while SMP 22 had been observed with the FOC.

SMP 1 and SMP 6 are small nebulae with very uncomplicated structures. The round (E?) morphology of these two targets was easily seen in the PC1 data set (Vassiliadis et al. 1998). The previous photometric radii measurements from SMP 1 and SMP 6 were 0.″12 and 0.″152, respectively, close to the current measurements of 0.″15 and 0.″19.

The situation of the bipolar PN SMP 22 is very different. The complete nebular morphology that we see in most emission lines of the STIS spectra, but in particular in the [N II] lines, is not as evident in the FOC image (Stanghellini et al. 1999); see Figure 5. Furthermore, we measure a photometric radius of 0.″4, while the radius from the FOC image is almost 3 times larger. We reanalyzed these measurements and noted that a radius of 0.″4 already included about 75% of the total flux, but to encircle 85% of the flux required a 1.″37 radius. From the comparison of the old and new SMP 22 images, we conclude that the main morphological features of Magellanic Cloud PNs are reliable from the pre-COSTAR images, even if the detailed morphology was not resolved. On the other hand, the measurements of the photometric radii are not reliable.

3.3. *Statistics of Morphological Types*

From our analysis we can see that SMC PNs are nicely classified using the same morphological scheme as the LMC and Galactic PNs. In order to increase the sample size for statistical purposes, we include in the present sample three additional SMC PNs described and classified in Stanghellini et al. (1999). After eliminating unresolved objects and repeats, we have at our disposal a sample of 30 SMC PNs whose morphology is well determined. This SMC PN sample constitutes nearly 50% of all known SMC PNs; thus, we consider it fairly representative at least of the bright PNs. In Table 4, we give the statistics of PN morphology for the SMC sample, as compared to the LMC and Galactic samples from Shaw et al. (2001).

The LMC and SMC samples in columns (2) and (3) of Table 4 have been selected in similar ways, and they have similar observational biases (but none of the extreme selection biases that affect Galactic PN samples toward the Galactic plane). While the fraction of round PNs remains more or less the same in the two samples, the fractions of

TABLE 4

PN Morphological Types: SMC versus LMC and Galaxy

Morphological Classification (1)	SMC (%) (2)	LMC (%) (3)	Galaxy (%) (4)
Round (R)	30	29	23
Elliptical (E)	37	17	49
Bipolar core (BC)	17	34	9
Bipolar (B)[a]	13	17	17
Point-symmetric (P)	3	3	3
Total, asymmetric[b]	30	51	26

[a] Includes quadrupolar PNs.

[b] Includes B and BC, but not P.

elliptical and bipolar core PNs in the SMC are, respectively, twice and one-half those in the LMC. The overall frequency of asymmetric PNs in the SMC is only 60% that of the LMC. This remarkable result strongly suggests that the difference between the Magellanic Clouds is reflected in their PN populations: something in the environment of the SMC may not be favorable to the formation of bipolar and bipolar core PNs. Alternately, this may be the result of the low metallicity of the SMC, indicating that the production of the higher mass progenitors of PNs in the SMC has long subsided and that the low percentage of asymmetric PNs in the SMC is due to the lack of recent star formation episodes. This issue will be better framed once we have complete abundance analysis for the PNs analyzed in this paper.

3.4. *Surface Brightness–Radius Relation*

We plot the surface brightness–to-radius relation for SMC (Fig. 8) and SMC and LMC PNs together, using the LMC data from Stanghellini et al. (2002) (Fig. 9). In Figures 8 and 9 the PNs are coded for their morphological types. We exclude from these plots round and elliptical PNs (both SMC and LMC) with inner (and outer) structure, to avoid possible misclassifications (see above). These figures confirm for SMC PNs the trend that we found for LMC PNs: surface brightness in the light of [O III] λ5007, Hα, Hβ, [O I] λ6300, [N II] λ6584, and [S III] λ6312 evolves differently for the different morphological types. The surface brightness–to-radius relation is very tight in all spectral lines, with the exception of the [N II] emission line, where a larger spread is present. From the bottom left panels of Figures 8 and 9, we see that the [N II] spread is more extreme for bipolar PNs. A possible factor is the higher but more varied nitrogen abundances of bipolar and bipolar core PNs.

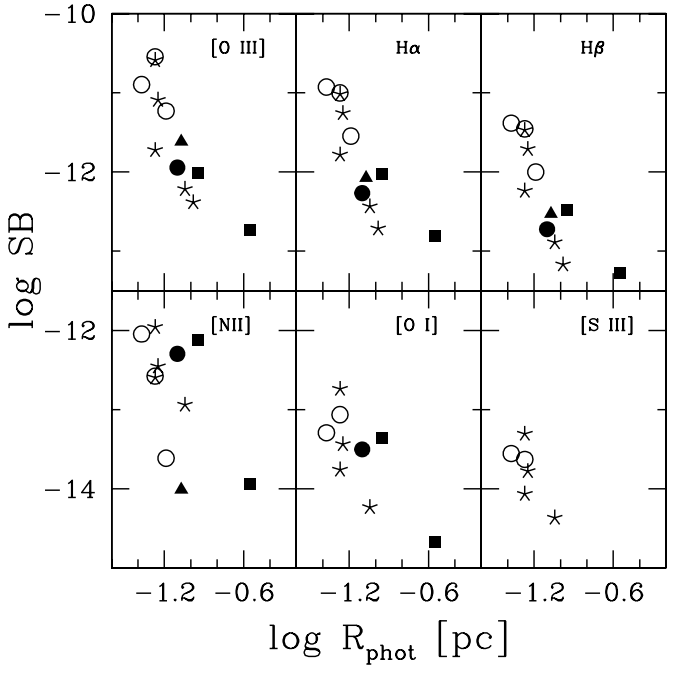

FIG. 8.—Surface brightness decline for the multiwavelength images of the PNs in our STIS survey. Emission lines in which the surface brightness is derived are indicated in the panels. Symbols indicate morphological types: round (*open circles*), point-symmetric (*filled circles*), elliptical (*asterisks*), bipolar core (*triangles*), and bipolar (and quadrupolar; *squares*). The photometric radii are measured from the [O III] λ5007 images, where available.

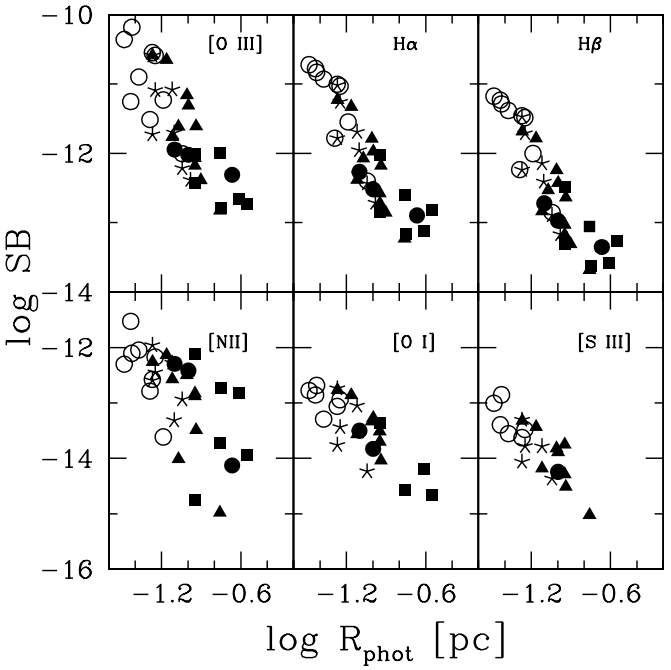

FIG. 9.—Same as Fig. 8, but for SMC and LMC PNs together (see text).

3.5. *The* [O III] λ5007/Hβ *Distribution*

In Figure 10, we plot a histogram of the ratio of reddening-corrected fluxes of the [O III] λ5007 and Hβ lines (hereafter [O III]/Hβ) for the PNs of the SMC and the LMC. The median of the SMC distribution is a factor of 2 lower than for the corresponding LMC distribution. Specifically, our

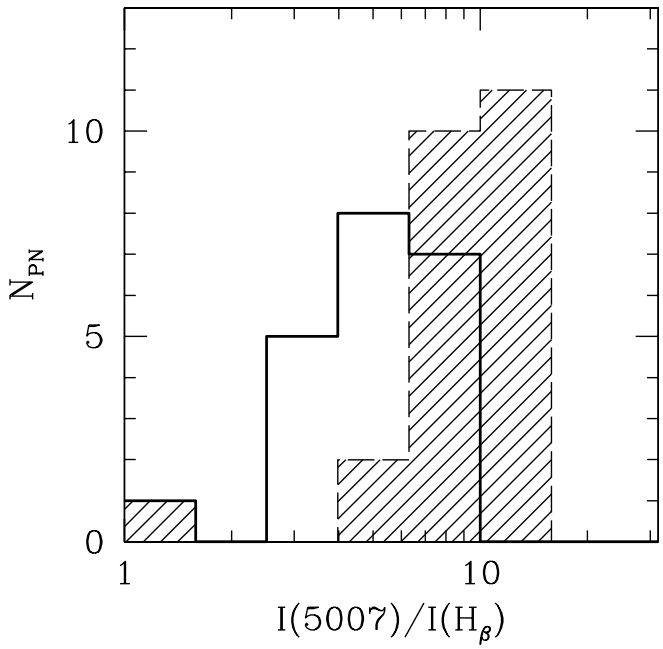

FIG. 10.—Distribution of the [O III] λ5007/Hβ intensity ratios in the SMC (*open histogram*) and LMC (*hatched histogram*) PNs.

TABLE 5
PHOTOIONIZATION MODELS, INPUT

Model	log(He/H)	log(C/H)	log(N/H)	log(O/H)	log $T_{\rm eff}$	log $L/L_{\odot}$
Galactic Models						
1	−1.0	−3.523	−4.0	−3.222	4.517	3.887
2	−1.0	−3.523	−4.0	−3.222	4.828	3.869
3	−1.0	−3.523	−4.0	−3.222	5.032	3.823
4	−1.0	−3.523	−4.0	−3.222	5.202	3.655
5	−1.0	−3.523	−4.0	−3.222	5.238	3.348
LMC Models						
6	−1.0	−3.380	−3.91	−3.644	4.569	3.973
7	−1.0	−3.380	−3.91	−3.644	4.797	3.964
8	−1.0	−3.380	−3.91	−3.644	5.024	3.932
9	−1.0	−3.380	−3.91	−3.644	5.233	3.805
10	−1.0	−3.380	−3.91	−3.644	5.298	3.481
SMC Models						
11	−1.03	−3.370	−4.57	−4.06	4.523	3.938
12	−1.03	−3.370	−4.57	−4.06	4.838	3.936
13	−1.03	−3.370	−4.57	−4.06	5.046	3.905
14	−1.03	−3.370	−4.57	−4.06	5.234	3.775
15	−1.03	−3.370	−4.57	−4.06	5.292	3.474

STIS data yield galaxy averages $\langle$[O III]/H$\beta\rangle_{\rm SMC} = 5.7 \pm 2.5$ and $\langle$[O III]/H$\beta\rangle_{\rm LMC} = 9.4 \pm 3.1$.

To the best of our knowledge, this result is free of object selection biases, since both sets of targets were chosen in much the same way. The objects with very low [O III]/Hβ ratios are very low ionization objects whose CSs are presumably too cool to form much O^{++}. However, the [O III]/Hβ ratio tends to reflect that of the PNs with the brightest [O III] and Hβ lines. In general, we tend to favor targets with the hottest CSs: $T_{\rm eff} \geq 50,000$ K.

The low median value of [O III]/Hβ in the SMC has been noted before, from ground-based measurements (Webster 1975). However, the STIS images allow us to distinguish between small, bright H II regions and PNs. Using the ground-based data from Stasińska, Richer, & McCall (1998), we derive substantially the same result: $\langle$[O III]/H$\beta\rangle_{\rm SMC} = 4.0 \pm 2.8$ and $\langle$[O III]/H$\beta\rangle_{\rm LMC} = 9.2 \pm 4.2$. For reference, the [O III]/Hβ ratio for Galactic PNs is on the order of 15.

The [O III]/Hβ emissivity ratio is physically scaled linearly with the O/H abundance and the fractional ionization of O^{++}. Also, it depends exponentially on the local electron excitation temperature, $T_e(O^{++})$, since electron collisions on the high-energy tail of the free energy distribution excite the transition. Of course, $T_e(O^{++})$ depends on O/H and O^{++}/O as well. So interpreting the differences between the [O III]/Hβ ratios of the SMC and the LMC is best done using ionization models.

We used the ionization model CLOUDY (Ferland 1996) to understand the systematic trends in the behavior of [O III]/Hβ for the SMC, the LMC, and the Galaxy. We adopted a gas density of 1000 cm^{-3} and standard chemical abundances for the three environments. Galactic abundances for the PNs of the Galaxy are those adopted in the Paris meeting (1985; see Table 7 in the Hazy manual; Ferland 1996). We used LMC average abundances of PNs quoted in Stanghellini et al. (2000) and SMC average abundances from Stasińska et al. (1998), except for the C/H ratio, which comes from Leisy & Dennefeld (1996), where we had selected from their Table 3 only the low-error data. The stellar ionizing spectrum is assumed to be a blackbody, with temperatures and luminosities from the H-burning evolutionary tracks for the appropriate galactic population by Vassiliadis & Wood (1994). Our model parameters are summarized in Table 5.

The predictions of [O III]/Hβ from CLOUDY models are shown in Figure 11 for the SMC, LMC, and Galactic PNs. The outcomes of the CLOUDY models are rather

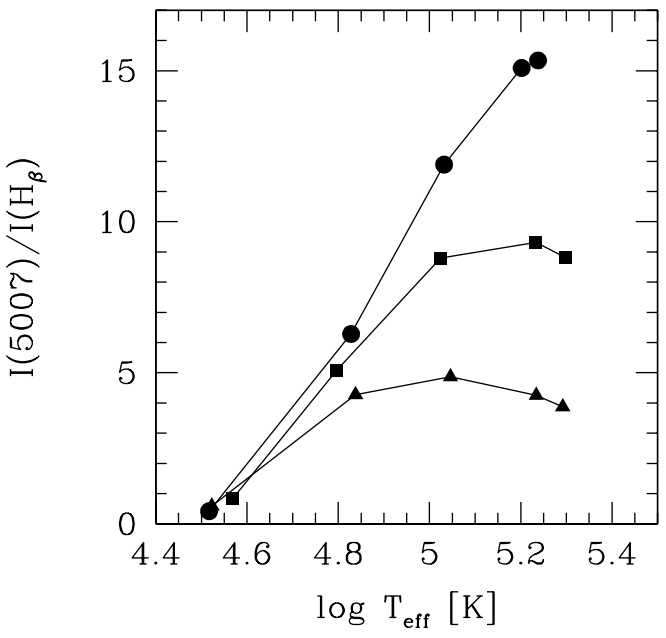

FIG. 11.—[O III] λ5007/Hβ intensity ratios for SMC (*triangles*), LMC (*squares*) and Galactic (*circles*) models. Temperatures reflect the evolution from the AGB to the maximum CS temperature in the evolutionary tracks of SMC, LMC, and Galactic post-AGB stars.

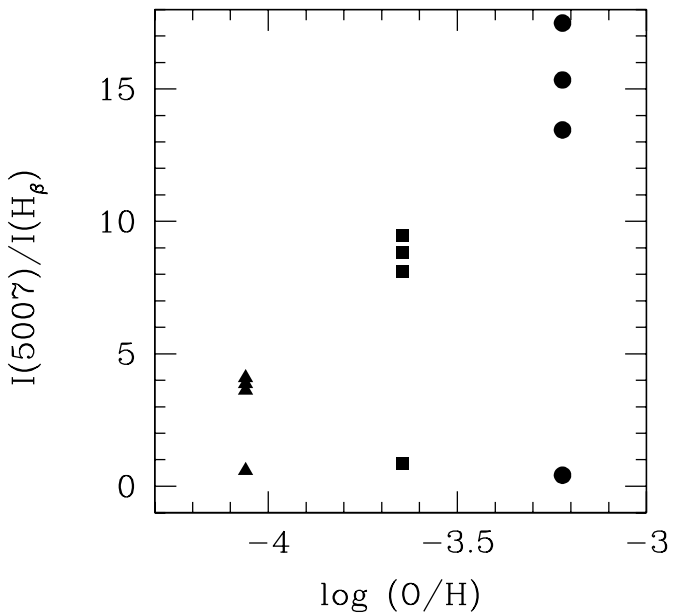

FIG. 12.—[O III] λ5007/Hβ intensity ratios vs. the oxygen abundances for SMC, LMC, and Galactic PNs. Symbols as in Fig. 11. PN models have constant density. We plot one cool model and a group of hot models for each galaxy. The three hot models represent three mean densities; see text.

insensitive to the adopted stellar properties and the assumed density (e.g., Fig. 12). But they are very sensitive to the adopted abundance ratios, especially the oxygen abundance. The model values of [O III]/Hβ are shown as a function of stellar temperature over the range of temperatures encountered by a star of mass 2 $M_{\odot}$, as it evolves from the AGB tip to its maximum post-AGB temperature. At stellar temperatures in excess of $\sim 10^5$ K, the [O III]/Hβ ratio is in rough agreement with the present observations (see also Garnett & Dinerstein 1988, 1989). It is worth noting that the Galactic models presented here are not to be compared directly with the known observed [O III]/Hβ distribution without accounting for selection effects that hamper Galactic PN statistics. We should clarify that the results of Figure 11 are valid for the input abundances. If, for example, we chose to use as input the average oxygen abundance for SMC PNs from Leisy & Dennefeld (1996) instead of that of Stasińska et al. (1998), the [O III]/Hβ emission-line ratio would be as high as 7.2.

The cooling processes that determine $T_e(O^{++})$ in the SMC, LMC, and Galactic PNs are noteworthy. In the Galaxy, the primary coolants of PNs with hot CSs are the optical forbidden lines of [O III] λ5007 and other lines of O^+ and O^{++}. However, in environments in which O/H is as low as in the SMC, the primary coolants may be ultraviolet intercombination lines of C^+ and C^{++}. It will be interesting to confirm these predictions with future UV observations.

Before reaching conclusions and further speculation, let us explore the weight of our assumptions. One is that these models have constant hydrogen density, which is arbitrarily assumed to be equal to 1000 cm^{-3}. By running CLOUDY for a constant-density model, the outer radius is determined by the Strömgen sphere. This makes our models larger as stellar temperature increases, reaching a maximum and then declining with the [O III] λ5007/Hβ intensity ratio. But in order to compare the radii of our models with our data, we should make a model for each nebula with the correct radius (i.e., assuming a density profile that reproduces that PN, for example, as determined in hydrodynamic calculations). This will be done in detail in a future paper. For now, let us examine what a difference in the average hydrogen density will make in the [O III] λ5007 flux ratio. In Figure 12, we plot the [O III]/Hβ ratio against the oxygen abundance for the early and the hottest models in the SMC (*triangles*), the LMC (*squares*), and the Galaxy (*circles*). The early models correspond to models 1, 6, and 11 of Table 5, with $\log N_{\rm H} = 3$ cm^{-3}. The hot models have been calculated for $\log N_{\rm H} = 2.5$, 3, and 3.5 cm^{-3}. We see that varying the density does not affect very much the studied intensity ratio, especially for the low-oxygen models. The different hot SMC models in Figure 12 are all within $\delta I(\lambda 5007)/I(\mathrm{H}\beta) = 1$, and their outer radii are 0.11, 0.25, and 0.55 pc for $\log N_{\rm H} = 3.5$, 3, and 2.5 cm^{-3}, respectively.

All models described in this paper have a filling factor (ϵ) equal to unity. Changing the value of the filling factor will also change the outer radius of the nebular models. For example, the hot Galactic model (with $\log N_{\rm H} = 3$) with $\epsilon = 0.5$ has an outer radius about 1.3 times larger than the model with $\epsilon = 1$. We find that the [O III] λ5007/Hβ intensity ratio with the different radius and filling factor is 95% of the ratio in the unity filling factor model; thus, the filling factor assumption is not very important in the discussion of the [O III] λ5007 line intensity with respect to Hβ.

Oxygen is usually the major coolant in the oxygen-abundant PNs. But what other coolants play a role? In Figure 13, we show the intensity of the line relative to Hβ for the major coolants in the SMC, LMC, and Galactic PNs, versus the oxygen abundance. The intensities are from the hottest models for each galactic mix. CLOUDY predicts that although the λ5007 line is the major coolant for the Galactic and LMC PNs, in the SMC PNs the [C IV] λ1550 line is the major coolant. Other carbon lines are also important coolant in the SMC PNs, while the [O III] λ4959 and [O II] λ3727 lines are significant mostly for the Galactic models. Clearly, more detailed models and observations of [C IV] $\lambda\lambda$1909 and 1550

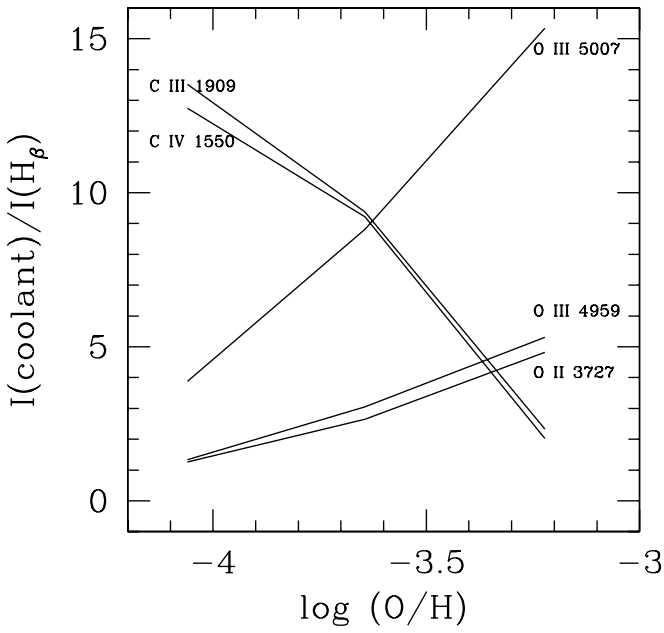

FIG. 13.—Intensity ratios of the major PN coolants to Hβ vs. oxygen abundances. The coolant is indicated in the right-hand side of the plot.

are essential to confirm these predictions, but the interpretation is plausible and consistent with the available data.

In Stanghellini et al. (2002), we used the I[O III] $\lambda\lambda$(5007+4959)/Hα ratio to trace the nebular excitation, and by inference the stellar temperature, of the LMC PNs. We cannot perform the same analysis for SMC PNs, since it is clear from Figure 11 that their [O III]/Hβ ratio–to-temperature relation is nonmonotonic.

3.6. *Electron Densities and Ionized Masses*

Table 6 lists nebular densities determined from strong [S II] $\lambda\lambda$6716, 6731 lines for eight SMC PNs (this paper) and 12 LMC PNs (Stanghellini et al. 2002). We assumed $T_e = 10^4$ K for these estimates. However, the derived densities are extremely insensitive to T_e (Osterbrock 1989). We find that $\langle N_e \rangle_{\rm SMC} = 3.45$, whereas $\langle N_e \rangle_{\rm LMC} = 3.28$, a factor 1.5 difference. Given the small sample size, a factor of 1.5 is not likely to be very significant. Furthermore, there is no discernible trend of N_e with morphological type in SMC or LMC PNs. Moreover, nebulae with bright [S II] lines are strongly biased to those of generally high fluxes or surface brightness or low ionization. These selection biases render trends in N_e of limited significance.

In addition, we estimate the masses of PNs in the LMC and SMC using the method of Boffi & Stanghellini (1994).

TABLE 6
Electron Density and Ionized Mass

Name	$\log N_e$ (cm^{-3})	$M_{\rm ion}$ ($M_\odot$)
SMC		
SMP 13	3.6	0.40
SMP 14	3.6	0.10
SMP 18	3.6	0.28
SMP 19	3.4	0.21
SMP 22	3.4	0.28
SMP 24	3.1	0.86
SMP 25	3.4	0.10
SMP 26	3.1	0.15
Average	3.4	0.30
LMC		
SMP 9	3.2	0.12
SMP 13	2.9	0.63
SMP 16[a]	2.9	0.33
SMP 19	3.4	0.21
SMP 28	3.2	0.10
SMP 30[a]	2.9	0.16
SMP 46	3.4	0.05
SMP 53	3.5	0.26
SMP 71	3.6	0.17
SMP-80	3.2	0.14
SMP 95[a]	2.9	0.16
SMP 100	3.4	0.17
Average[b]	3.3	0.21

[a] Possible overlap of the [S II] $\lambda\lambda$6716 and 6731 lines, uncertain electron density and ionized mass.

[b] Does not include PNs with uncertain ratios (see footnote a).

The average ionized mass of the eight SMC PNs, 0.3 $M_\odot$, is slightly larger than that of LMC PNs, 0.2 $M_\odot$. Given the uncertainty in the data and the small data sample, we do not believe that the mass discrepancy between SMC and LMC PNs is significant. Also, we fail to see any obvious trend between nebular mass and morphological type.

4. SUMMARY AND CONCLUSIONS

A sample of 27 SMC PNs has been observed in imaging and slitless mode with *HST*/STIS to examine their morphology, shape, and fluxes and to study their evolution. This morphological sample is the first sizable set of SMC PNs and represents almost half of the known SMC PNs. The images and spectra have the same high quality and resolution as our LMC sample. We present the broadband and monochromatic images in the major emission lines and determine that morphology is easily recognized in most emission lines. We find that the ratio of symmetric to asymmetric PNs is remarkably different in the SMC and the LMC. Specifically, bipolar PNs are much rarer in the SMC than in the LMC (or the Galaxy). This new result has significant implications for the relation between stellar population and PN morphology. It is well known from Galactic and LMC PN studies that PN morphology correlates with the mass of the progenitor stars. In particular, bipolar PNs evolve from relatively massive ($\geq$1.5 $M_\odot$) progenitors. Thus, the low incidence of bipolar PNs in the SMC probably reflects the low formation rate of these stars in the past $\geq$5 Gyr. This is in accord with other studies of star formation rates in the LMC and the SMC. Alternately, or in addition, the low metallicity of the SMC may inhibit wind collimation somehow.

We also present the measurement of the optical line intensities. We find that the surface brightness declines with radii in most emission lines, adding value to the possible calibration of the surface brightness–nebular radius correlation seen in the LMC. Ionized masses and electron densities were calculated where the [S II] doublet intensity was available. The resulting ionized masses do not seem to have a relation to the morphology, as already found in the LMC PNs.

The [O III]/Hβ ratio of Magellanic Cloud PNs has been studied in detail. The factor of 2 difference between the LMC and SMC PNs was modeled with CLOUDY. We find that the cooling models strongly depend on the oxygen content and that the brightest parts of the [O III] λ5007/Hβ luminosity function shift between SMC and LMC PNs. We also find a relation between the brightest [O III] λ5007/Hβ PNs and their morphology, which is different for each Magellanic Cloud population.

We thank George Jacoby and Orsola de Marco for discussing the faint-target selection, Orsola de Marco for her help in completing Phase II of the *HST* program, and Massimo Stiavelli for his suggestions about CLOUDY models. This work was supported by NASA through grant GO-08663.01-A from the Space Telescope Science Institute, which is operated by the Association of Universities for Research in Astronomy (AURA), Inc., under NASA contract NAS 5-26555.

REFERENCES

Boffi, F. R., & Stanghellini, L. 1994, A&A, 284, 248
Boroson, T. A., & Liebert, J. 1989, ApJ, 339, 844
Dopita, M. A., & Meatheringham, S. J. 1990, ApJ, 357, 140
———. 1991a, ApJ, 367, 115
———. 1991b, ApJ, 377, 480
Ferland, G. J. 1996, Hazy, a Brief Introduction to CLOUDY (Lexington: Univ. Kentucky Dept. Phys. and Astron.)
Garnett, D. R., & Dinerstein, H. L. 1988, AJ, 95, 119
———. 1989, PASP, 101, 541
Leisy, P., & Dennefeld, M. 1996, A&AS, 116, 95
Manchado, A., Guerrero, M., Stanghellini, L., & Serra-Ricart, M. 1996, The IAC Morphological Catalog of Northern Galactic Planetary Nebulae (La Laguna: IAC)
McGrath, M. A., Busko, I., & Hodge, P. E. 1999, STIS Instrum. Sci. Rep. 99-03 (Baltimore: STScI)
Meyssonnier, N., & Azzopardi, M. 1993, A&AS, 102, 451
Osterbrock, D. E. 1989, Astrophysics of Gaseous Nebulae and Active Galactic Nuclei (Mill Valley: University Science Books)
Shaw, R. A., Stanghellini, L., Mutchler, M., Balick, B., & Blades, J. C. 2001, ApJ, 548, 727
Stanghellini, L., Blades, J. C., Osmer, S. J., Barlow, M. J., & Liu, X. W. 1999, ApJ, 510, 687
Stanghellini, L., Corradi, R. L. M., & Schwarz, H. E. 1993, A&A, 279, 521
Stanghellini, L., Shaw, R. A., Balick, B., & Blades, J. C. 2000, ApJ, 534, L167
Stanghellini, L., Shaw, R. A., Mutchler, M., Palen, S., Balick, B., & Blades, J. C. 2002, ApJ, 575, 178
Stasińska, G., Richer, M. G., & McCall, M. L. 1998, A&A, 336, 667
Vassiliadis, E., Dopita, M. A., Morgan, D. H., & Bell, J. F. 1992, ApJS, 83, 87
Vassiliadis, E., & Wood, P. R. 1994, ApJS, 92, 125
Vassiliadis, E., et al. 1998, ApJ, 503, 253
Webster, B. L. 1975, MNRAS, 173, 437